PROCEEDINGS, 45th Workshop on Geothermal Reservoir Engineering
Stanford University, Stanford, California, February 10-12, 2020
SGP-TR-216

Thermo-Fluid-Structure Interaction Based on the Fictitious Domain Method: Application to Dry Rock Simulations

Nasibeh Hassanjanikhoshkroud[1,4], Maria G. C. Nestola[1,2], Patrick Zulian[1], Cyrill Von Planta[1], Daniel Vogler[3], Harald Köstler[4], Rolf Krause[1]

[1]Institute of Computational Science, USI, Via Giuseppe Buffi 13, 6900, Lugano Switzerland

[2]Institute of Geochemistry and Petrology, ETH Zurich, Clausiusstr. 25, 8092 Zurich, Switzerland

[3]Institute of Geophysics, ETH Zurich, Sonneggstr. 5, 8092 Zurich, Switzerland

[4]Institute of System Simulation, FAU, Cauerstraße 11, 91058, Erlangen Germany

nasibeh.hassanjani@gmail.com

Keywords: Thermal-fluid-structure interaction, enhanced geothermal systems, fictitious domain method, variational transfer.

ABSTRACT

Enhanced Geothermal Systems (EGS) generate geothermal energy without the need for natural convective hydrothermal resources by enhancing permeability through hydraulic fracturing. EGS involve complex and highly nonlinear multiphysics processes and face several technical challenges governing productivity and associated risks in a wide range of reservoir engineering problems. Numerical simulations offer a unique opportunity to improve the hydraulic stimulation design and investigate their long-term performance. In this work, we present a thermo-hydro-mechanical coupling based on the fictitious domain method. Fictitious domain methods include nonconforming mesh approaches that rely on the use of different discretizations for the solid and the fluid domain. We consider the governing equations of linear thermo-elasticity to model the heat transfer in dry and hot rocks. Navier-Stokes equations and heat convection equations are adopted for describing the thermal flux in an incompressible fluid flow. The two problems are coupled in a staggered manner through the variational transfer. Indeed, the use of the variational transfer allows simplifying the setup of fracture simulations with complex surfaces embedded in the fluid domain, thus avoiding the inconvenient mesh generation required by the boundary fitted methods. The presented computational framework is first verified with analytical two-dimensional benchmarks, and then employed to simulate the thermo-hydro-mechanical coupling between fluid and idealized fracture asperities.

1. INTRODUCTION

Thermal-Fluid-Structure Interaction (TFSI) is an essential process in enhanced geothermal systems (EGS) and also in the engineering of them (Li et al. 2016; Cacace and Jacquey 2017; Li et al. 2019; Lima et al. 2019). Thus, numerical simulations may play a crucial role in understanding fluid flow through fractured rocks under thermo-hydro-mechanical conditions. In this regard, numerical models of fractured reservoirs have become an increasingly active area of research (Yin and Liu 2015; Li et al. 2016; Cacace and Jacquey 2017; Li et al. 2019) mainly due to the computational and numerical challenges arising from the complex and nonlinear multiphysics processes occurring in EGS (Taron and Elsworth 2009, Vogler et al. 2018).

In the literature, several methods have been introduced, which can be classified in conforming and non-conforming approaches. The complexity of conforming approaches is related to the mesh generation, whereas non-conforming mesh methods require the use of specific numerical techniques such as mortar methods, extended finite element discretizations, and PDE constrained optimization.

The approach presented in this contribution is inspired by the fictitious domain (FD) method, which has been introduced in (Glowinski et al. 1999) to simulate the movement of particles into a fluid and then extended to elastic bodies in (Yu et al. 2005). The main advantage of the FD approach is that it allows for the discretization of the fluid problem on a fixed grid by adopting an Eulerian description, whereas the solid structure is tracked in a Lagrangian fashion. The coupling conditions between the two physics is prescribed on the fluid-solid interface (Glowinski et al. 1999) or over the entire overlapping region (Boffi et al. 2003; Hesch et al. 2014) by using Lagrange multipliers or penalization techniques.

In this paper, we present a Thermo-Fluid-Structure interaction approach, which relies on the fluid-structure interaction (FSI) formulation introduced in (Nestola et al. 2016) to model hyperelastic structures embedded in complex flows, and recently employed in (Planta et al. 2019) for the simulation of fluid flow in fracture asperities. These FSI methodologies are further extended to model the heat conduction in the solid, the heat convection in the fluid flow, and the heat exchange between the two physics.

In particular, we employ a staggered strategy where all physical quantities of interest are transferred between the fluid and the solid mesh through the fully parallel variational approach proposed in (Zulian et al. 2016). We employ a penalization technique to couple the Navier-Stokes equations with the constraints prescribing continuity of temperature and velocity. Moreover, the solid mechanics equations are slightly modified to include the force exerted by the fluid to the solid, and the heat exchanged between the two physics.

The proposed methodology is verified with analytical benchmarks and finally employed to simulate fluid flow and heat transfer in simplified fracture asperities.

2. THERMO-FLUID-STRUCTURE-INTERACTION

The key ingredients of the proposed TFSI framework are 1) the thermo-elasticity problem, 2) the thermo-fluid dynamics equations, and 3) the coupling of the two subproblems.

2.1 Thermo-elasticity problem

Thermo-elasticity is the study of the elastic behavior of a body subject to temperature changes and prescribed external forces. In particular, we restrict our attention to linear elastic materials, such as fractured rocks, whose deformations are linearly proportional to the magnitude of applied stress.

We define $\Omega_s \subset R^n, n \in \{2,3\}$ as a bounded domain representing the region occupied by the solid body whose boundary $\partial\Omega_s$ is split into the Dirichlet $\partial\Omega_{Ds}$ and Neumann $\partial\Omega_{Ns}$ parts such that $\partial\Omega_{Ds} \cup \partial\Omega_{Ns} = \partial\Omega_s$ and $\partial\Omega_{Ds} \cap \partial\Omega_{Ns} = \emptyset$ (as shown in Figure 1). The displacement field d_s and the temperature field T_s of a solid structure are obtained by solving the following equations (Nowinski 1978; Danowski et al. 2013):

$$\rho_s \ddot{d}_s - \nabla \cdot \sigma_s = \rho_s F_s \qquad in\ \Omega_s \tag{1}$$

$$\rho_s c_s \dot{T}_s + \nabla \cdot (-k_s \nabla T_s) - T_{ref}\, \beta I : \dot{\varepsilon}_m = 0 \qquad in\ \Omega_s \tag{2}$$

$$\sigma_s = 2\mu\varepsilon_m + \lambda tr(\varepsilon_m) I + \beta I (T_s - T_s^*) \tag{3}$$

$$d_s = d_{Ds}, \qquad T_s = T_{Ds} \qquad on\ \partial\Omega_{Ds} \tag{4}$$

$$\sigma_s n_s = \bar{t}_{Ns}, \qquad \frac{\partial T_s}{\partial n} = q_{Ns} \qquad on\ \partial\Omega_{Ns} \tag{5}$$

$$d_s = d_0 s, \qquad u_s = \dot{d}_{0s}, \qquad T_s = T_{0s} \qquad t = 0\ \ \forall x \in \Omega_s \tag{6}$$

where ρ_s is the density, $u_s = \dot{d}_s$ is the solid velocity vector field, σ_s is the solid Cauchy stress tensor, ε_m is the linear strain tensor, F_s is a volumetric density force, c_s is the heat capacity, α is the thermal expansion coefficient, $\beta = -(2\mu + 3\lambda)\alpha$ is the stress-temperature modulus, T_s is the temperature field, T_s^* is a prescribed stress-free temperature, I is the second rank identity tensor, k_s is the heat conductivity (here assumed homogeneous and isotropic), t is the time and n_s is the outward unit normal to the boundary. The superscript ($\dot{}$) and ($\ddot{}$) refer to the first and second time-derivatives, respectively. Displacement d_{Ds} and temperature T_{Ds} are the prescribed values on the Dirichlet boundary. Boundary traction $\bar{t}_{Ns}$ and heat flux q_{Ns} are prescribed values on the Neumann boundary. Moreover, d_{0s}, $\dot{d}_{0s}$, and T_{0s} are the initial conditions for displacement, velocity, and temperature, respectively.

2.2 Thermo-fluid dynamics problem

We introduce the Navier-Stokes (NS) equations defined in a Eulerian framework and couple them with the energy equation to model heat transfer within a fluid. We restrict our attention to incompressible Newtonian flows.

Let $\Omega_f \subset R^n, n \in \{2,3\}$ be a bounded fluid domain whose boundary $\partial\Omega_s$ is split into the Dirichlet $\partial\Omega_{Df}$ and Neumann $\partial\Omega_{Nf}$ parts such that $\partial\Omega_{Df} \cup \partial\Omega_{Nf} = \partial\Omega_f$ and $\Omega_{Df} \cap \partial\Omega_{Nf} = \emptyset$ (as shown in Figure 2). The pressure field p_f, the velocity field u_f, and the temperature field T_f are obtained by solving the following equations (Anderson and Wendt 1995):

$$\nabla \cdot u_f = 0 \qquad in\ \Omega_f \tag{7}$$

$$\rho_f \dot{u}_f + \rho_f (u_f \cdot \nabla u_f) - \nabla \cdot \sigma_f = \rho_f F_f \qquad in\ \Omega_f \tag{8}$$

$$\rho_f c_f \left(\dot{T}_f + u_f \cdot \nabla T_f\right) + \nabla \cdot (-k_f \nabla T_f) - \sigma_f : \nabla u_f = 0 \qquad in\ \Omega_f \tag{9}$$

$$\sigma_f = -p_f I + \mu_f \left(\nabla u_f + \nabla u_f{}^T\right) \tag{10}$$

$$u_f = u_{Df}, \qquad T_f = T_{Df} \qquad on\ \partial\Omega_{Df} \tag{11}$$

$$\sigma_f n_f = \bar{s}_{Nf}, \qquad \frac{\partial T_f}{\partial n} = q_{Nf} \qquad on\ \partial\Omega_{Nf} \tag{12}$$

$$u_f = u_{0f}, \qquad T_f = T_{0f} \qquad t = 0\ \ \forall x \in \Omega_f \tag{13}$$

where σ_f is the Cauchy stress for Newtonian fluids, F_f is a volumetric density force, ρ_f is the fluid density, μ_f is the fluid viscosity, k_f is the fluid heat conductivity (here assumed homogeneous and isotropic), c_f is the fluid heat capacity, I is the identity tensor, t is the

time and n_f is the outward unit normal to the fluid boundary. The superscript (˙) refers to the first time-derivative. The velocity u_{Df} and the temperature T_{Df} are the prescribed values at the Dirichlet boundary. The stress $\bar{s}_{Nf}$ and the heat flux q_{Nf} are prescribed values at the Neumann boundary. The initial values of the velocity vector field and temperature field are defined by u_{0f} and T_{0f}, respectively.

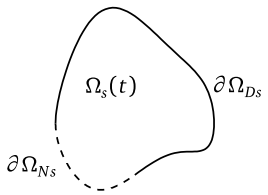

Figure 1: Solid domain.

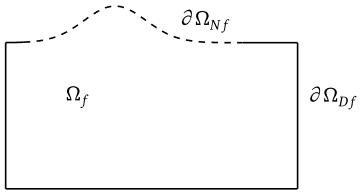

Figure 2: Fluid domain.

2.3 Coupling conditions

Similar to former FSI approaches based on the fictitious domain (Hesch et al. 2014; Nestola et al. 2019; Planta et al. 2019), the solid and fluid dynamics problems are solved on different domains, and then coupled through proper constraints imposed on the overlapping region, i.e. the region shared by the fluid and the solid. This is done in a staggered manner by means of a fixed-point iteration scheme to satisfy the coupling conditions. The fluid problem is formulated in Eulerian coordinates, while the solid problem is formulated in Lagrangian coordinates. We employ a penalization technique to couple the Navier-Stokes equations with the constraints prescribing continuity of temperature and velocity over the entire overlapping region (Planta et al. 2019). Then, we modify the solid mechanics equations to include the forces exerted by the fluid to the solid to reach the mechanic equilibrium, and the heat transferred from the fluid to the solid to reach the thermodynamic equilibrium. According to (Hesch et al. 2014) the inertial terms of the solid problem are evaluated by using the difference between the solid and the fluid density. The internal stresses and heat conduction of the fluid should also be subtracted from the solid contributions. However, this operation can be neglected in most applications since internal fluid stresses and fluid conductivity are considerably smaller than their solid counterparts.

2.3.1 Strong formulation

We embed the current configuration of the solid domain $\Omega_s(t)$ into the fluid domain Ω_f such that $\partial\Omega_f \cap \partial\Omega_s(t) = \emptyset$ (Figure 3), and denote the overlapping region as $\Omega_{fsi}(t) = \Omega_f \cap \Omega_s(t)$. The coupling TFSI conditions read as follows

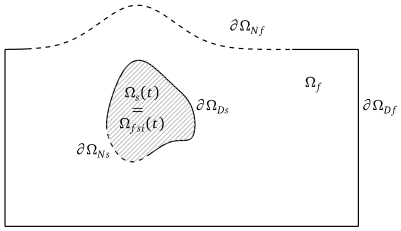

$$u = u_s \qquad in\ \Omega_{fsi}(t) \qquad (14)$$

$$T_f = T_s \qquad in\ \Omega_{fsi}(t) \qquad (15)$$

$$F_{f\to s} + F_{s\to f} = 0 \qquad in\ \Omega_{fsi}(t) \qquad (14)$$

$$Q_{f\to s} + Q_{s\to f} = 0 \qquad in\ \Omega_{fsi}(t) \qquad (15)$$

Figure 3: TFSI scenario with a solid domain $\Omega_s(t)$ embedded in a fluid domain Ω_f

Here $F_{f\to s}$ and $F_{s\to f}$ are the forces exerted by the fluid to the solid and from the solid to the fluid, respectively, whereas $Q_{f\to s}$ and $Q_{s\to f}$ is the heat exchanged from the fluid to the solid, and viceversa. Equations (14) and (15) ensure the mechanic and the thermodynamic equilibrium, respectively.

2.3.2 Weak formulation

Let us introduce the following function spaces:

$$S^d(\Omega_s) = \{v_m \in V_{\Omega_s} | v_m = 0\ \ on\ \ \partial\Omega_{Ds}\} \qquad S^{T_s}(\Omega_s) = \{v_T \in V_{\Omega_s} | v_T = 0\ \ on\ \ \partial\Omega_{Ds}\}$$

$$S^p(\Omega_f) = \{w_p \in W_{\Omega_f} | w_p = 0\ \ on\ \ \partial\Omega_{Df}\} \qquad S^{T_f}(\Omega_f) = \{w_T \in W_{\Omega_f} | w_T = 0\ \ on\ \ \partial\Omega_{Df}\} \qquad S^u(\Omega_f) = \{w_u \in W_{\Omega_f} | w_u = 0\ \ on\ \ \partial\Omega_{Df}\}$$

Then, the weak formulation of the TFSI problem reads as follows:

$$\int_{\Omega_s(t)} (\rho_s - \rho_f)\ddot{d}_s \cdot v_m dV + \int_{\Omega_s(t)} \sigma_s : \nabla v_m dV - \int_{\partial\Omega_{Ns}(t)} \bar{t}_{Ns} \cdot v_m dA - \int_{\Omega_s(t)} \rho_s F_s \cdot v_m dV - \int_{\Omega_{fsi}(t)} F_{f\to s} \cdot v_m dV = 0 \qquad (18)$$

$$\int_{\Omega_s(t)} (\rho_s - \rho_f) c_s \dot{T}_s v_T dV - \int_{\Omega_s(t)} T_{ref}\, \beta I : \dot{\varepsilon}_m\, v_T + \int_{\Omega_s(t)} k_s \nabla T_s \cdot \nabla v_T dV - \int_{\partial\Omega_{Ns}(t)} \bar{q}_{Ns} v_T dA - \int_{\Omega_{fsi}(t)} Q_{f\to s} \cdot v_T dV = 0 \quad (19)$$

$$\int_{\Omega_f} (\nabla \cdot u_f) w_p dV = 0 \quad (20)$$

$$\int_{\Omega_f} \rho_f (\dot{u}_f + \rho_f (u_f \cdot \nabla u_f)) \cdot w_u dV - \int_{\Omega_f} p_f \nabla \cdot w_u dV + \int_{\Omega_f} \mu_f \nabla u_f \cdot \nabla w_u dV - \int_{\Omega_f} F_f \cdot w_u dV - \int_{\partial\Omega_{Ns}} \bar{s}_{Nf} \cdot w_u dA + \int_{\Omega_{fsi}(t)} \epsilon_v^{-1} (u_f - u_s) w_u dV = 0 \quad (21)$$

$$\int_{\Omega_f} \rho_f c_f (\dot{T}_f + u_f \cdot \nabla T_f) w_T dV + \int_{\Omega_f} k_f \nabla T_f \cdot \nabla w_T dV - \int_{\Omega_f} \Phi w_T dV - \int_{\partial\Omega_{Nf}} q_{Nf} w_T dA + \int_{\Omega_{fsi}(t)} \epsilon_T^{-1} (T_f - T_s) w_T dV = 0 \quad (22)$$

where $\Phi = \sigma_f : \nabla u_f$ is the viscous dissipation in the fluid flow. As already mentioned, a penalty formulation is adopted to enforce the constraints (12) and (13) with ϵ being the penalty parameter.

2.3.3 Space and time discretization of the TFSI problem

For both the solid and the fluid problems we use the finite-element method for the spatial discretization. We use the Newmark method for the time discretization of the linear momentum equation of the solid problem and the implicit-Euler method for the time discretization of the remaining equations.

2.3.4 Variational transfer

As previously mentioned, we solve for the thermo-elasticity and the thermo-fluid dynamics problems separately on each domain. Consequently, discrete fields need to be transferred between non-matching meshes/discretizations. This is achieved by using the parallel variational transfer algorithms presented in (Krause and Zulian 2016). Let us define a function space V, with basis-functions v, over the solid domain $\Omega_s(t)$ and a function space W, with basis-functions w, over the fluid domain Ω_f such that $V \subset W$ and L^2 scalar product $(v, w)_{L^2} = \int_W vw\, dw$, is well defined. Let $\Pi : V \to W$, be the L^2-projection, such that the weak-equality condition $\int_{\Omega_{fsi}} (\Pi(v) - v)\mu\, dw = 0$ holds for all $v \in V$, $\mu \in M$, where M is a suitable Lagrange multiplier space. The discrete algebraic counterpart of the L^2-projection Π is encapsulated by the matrix P.

2.4 Algorithm

The coupled TFSI problem is solved with a fixed-point iteration algorithm at each time step. For a more concise exposition we drop all the indices connected to the time discretization and the fixed-point iteration, except where it is necessary.

Algorithm: Fixed-point iteration

Initialization: $l = 1, d = d_0, T_s = T_{s,0}, u = u_0, p = p_0, T_f = T_{f,0}$

for $l = 1,2, \ldots, L_{FP}$

Transfer $F_{f\to s}$ and $Q_{f\to s}$ from the fluid to the solid domain by setting: $z^*_{f\to s} \coloneqq P^T z_{f\to s}$, $\coloneqq$

Solve solid problem.

Transfer u_s, T_s to the fluid domain by setting: $(y)^*_s \coloneqq P(y)_s$

Solve fluid problem,

if $\frac{|y_s^{l-1} - y_s^l|}{|y_s^{l-1}|} \leq \mathrm{tol}_{\mathrm{FP}}$

end for

Algorithm provides an overview of the staggered approach where y_s is the solution field of the solid problem, and $z_{f\to s}$ refers to the reaction force exerted by the fluid to the solid, and the heat exchanged between the two physics. The superscript * refers to the projected values, whereas L_{FP} denotes the maximum number of iterations.

2.5 Implementation

Numerical simulations are carried out by using the open-source software library Utopia (Zulian et al. 2016) and MOOSE (Multiphysics Object Oriented Simulation Environment) framework (Gaston et al. 2009). The variational transfer is implemented in Utopia which makes use of LibMesh (Kirk et al. 2006) for the finite element discretization and MOONoLith (Zulian 2016) for the intersection detection.

3. NUMERICAL VERIFICATION

We present three benchmarks to verify the TFSI approach presented in this contribution. The first benchmark is the Couette flow. For this experiment, we consider a one-way interaction where only the fluid is affected by the solid. The second benchmark consists of a fully coupled problem with two overlapping square domains, one representing the solid and the other the fluid. The third benchmark is used to analyze the behavior of heat transfer under different fluid flow regimes.

3.1 Couette flow

We consider a solid plate that moves horizontally with a constant speed of $0.05\ m/s$ on top of the channel. The temperature of the solid is kept fixed (Ts=$283\ K$). We prescribe no-slip boundary conditions and impose a temperature equal to $273\ K$ at the bottom of the fluid channel. Details on the simulation set-up and the material properties are given in Figure 4 and Table 1, respectively. The penalty parameter is set equal to 10^{-6}.

For visualization purposes, we analyze the two physics separately in Figure 5. In particular, Figure 5(a) shows the velocity fields of the fluid (on the right) and the solid (on the left) when steady-state conditions are achieved, whereas the temperature distribution is depicted in Figure 5(b). One may observe that both the velocity and the temperature constraints are properly enforced in the overlapping region.

property	solid	fluid
density $(\rho)(kg/m^3)$	2710	1000
viscosity $(\mu)(Pa \cdot s)$	-	1
heat capacity $(c)\big(j/(kg \cdot k)\big)$	921	4200
heat conductivity $(k)\big(w/(m \cdot k)\big)$	237	0.1
Young's modulus $(E)(GPa)$	69	-
Poisson ratio $(\nu)(-)$	0.3	-

Table 1: Fluid and solid material properties

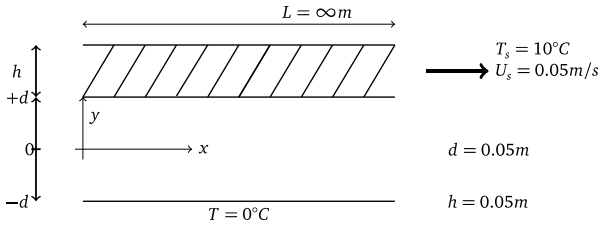

Figure 4: Set-up for the Couette flow benchmark.

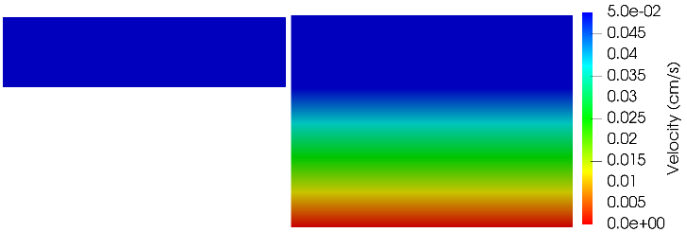

(a)

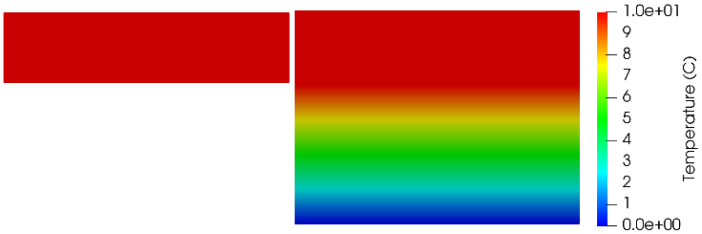

(b)

Figure 5: Velocity (a) and temperature (b) of the Couette flow benchmark for the solid domain (left) and the fluid domain (right).

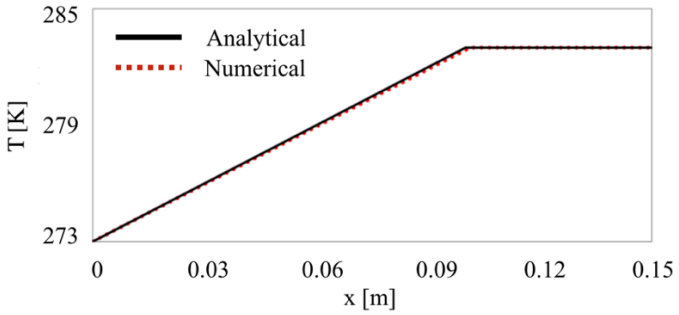

Figure 6: Temperature profile across the flow channel. The x axis represents the distance from the bottom of the channel (meters).

Figure 6 presents a comparison between the numerical velocity profile analyzed in the middle of the fluid channel and the analytical solution. The good agreement between the two profiles shows the capability of our TFSI approach to enforce the equality of the discrete fields over the overlapping region in an accurate way without the need of any re-meshing tool.

3.2 Two-square blocks

A fully coupled strategy is verified through a benchmark (Pironkov et al. 2010) consisting of two square domains (Figure 7). The right square is a solid block, and the left square is occupied by the fluid. The left and right Dirichlet boundaries have constant temperature values, equal to $300\,K$ and $310\,K$, respectively. The fluid is modeled as stationary (we impose no-slip conditions on the entire boundary) and the solid is modeled as a rigid structure. The simulation setup and material properties are given in Figure 7 and Table 2, respectively. Due to the temperature gradient, heat is conducted along the axial direction until the thermodynamic equilibrium is reached. The analytical solutions for the steady-state temperature of the solid and fluid, respectively, are: $T_{solid} = 1.32x + 309.736, T_{fluid} = 98.68x + 300$, where x is the axial coordinate starting from the left side of the fluid domain. Figure 8 depicts the steady-state temperature profiles in the axial direction at the mid-height of the two squares. The error computed by using the L-infinity norm is about ~ 10^{-5}. The good agreement between the numerical and the analytical solutions shows the capability of the overall TFSI framework to model complex scenarios where a fully coupled interaction between the solid and fluid phases is considered.

property	solid	fluid
density $(\rho)(kg/m^3)$	7800	1.255
viscosity (μ)$(Pa \cdot s)$	-	1.8×10^{-5}
heat capacity $(c)\big(j/(kg \cdot k)\big)$	450	1003
heat conductivity $(k)\big(w/(m \cdot$	45	2.5×10^{-2}
Young's modulus $(E)(GPa)$	2.1×10^{11}	-
Poisson ratio (ν)$(-)$	0.3	-

Table 2: Fluid and solid material properties.

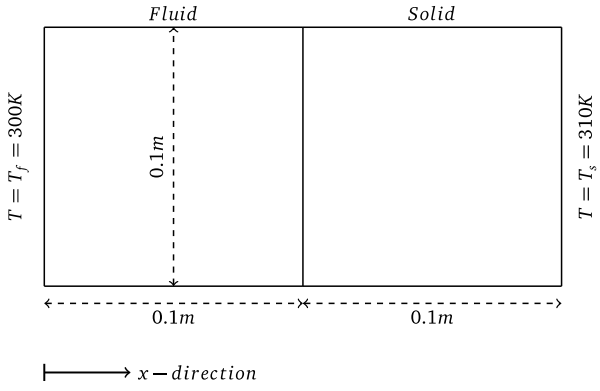

Figure 7: Set-up for the two-square blocks benchmark.

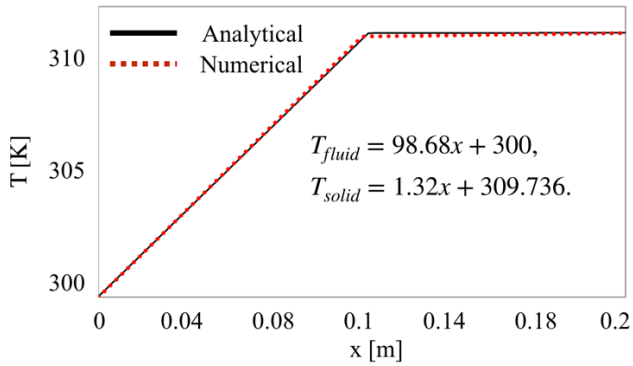

Figure 8: Temperature profile along the axial direction evaluated at the mid-height of the two squares.

3.3 Flow regime study

We consider two obstacles embedded in a two-dimensional fluid channel where the fluid has an initial temperature equal to 550 K. We impose zero displacement at the bases of the two obstacles and a constant temperature equal to 300 K. The simulation setup and material properties for the solid and the fluid domains are given in Figure 9 and Table 3. The fluid has parabolic velocity at inlet defined as: $u_f = v_m(0.1 - y)y$, where u_f is the fluid velocity, y is the distance from the bottom of the channel.

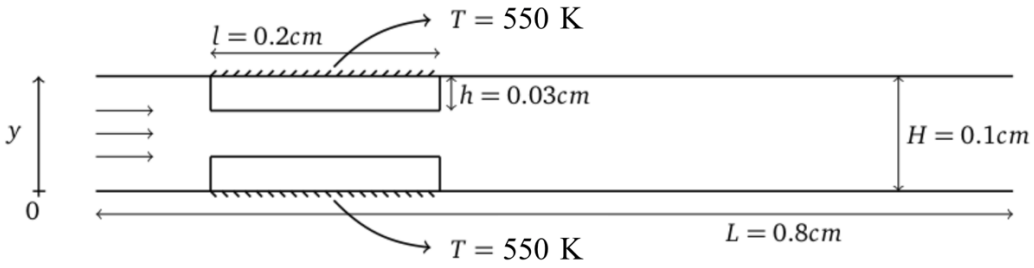

Figure 9: Set-up for the simulation of two obstacles in a flow-channel.

We analyze three different flow regimes, *slow*, *moderate,* and *fast*, obtained by assigning to the parameter v_m values equal to 5, 250, and 500 cm/s, respectively. Figure 10 shows the fluid velocity streamlines for all three scenarios at time $t = 0.20\ s$. The *fast* fluid regime (Figure 10 bottom) reaches the maximum velocity of about 3.0 cm/s, at the center of the fracture aperture. Then, as the fluid reaches the wider section, the velocity decreases and finally stays constant close to the outlet. The same trend can be observed for both the *slow* and the *moderate* fluid regimes (Figure 10 top and Figure 10 middle, respectively), where a maximum velocity of about 1.6 cm/s and 0.03 cm/s is reached, respectively. Figure 11 shows the velocity profile at the inlet of the fluid channel for all the flow regimes. It can be observed that a parabolic profile is obtained in agreement with the Poiseuille flow model.

property	**solid**	**fluid**
density $(\rho)(kg/m^3)$	1200	1000
viscosity $(\mu)(Pa \cdot s)$	-	0.001
heat capacity $(c)\big(j/(kg \cdot k)\big)$	790	4200
heat conductivity $(k)\big(w/(m \cdot k)\big)$	3.2	0.6
Young's modulus $(E)(GPa)$	10^5	-
Poisson ratio $(\nu)(-)$	0.4	-

Table 3: Fluid and solid material properties.

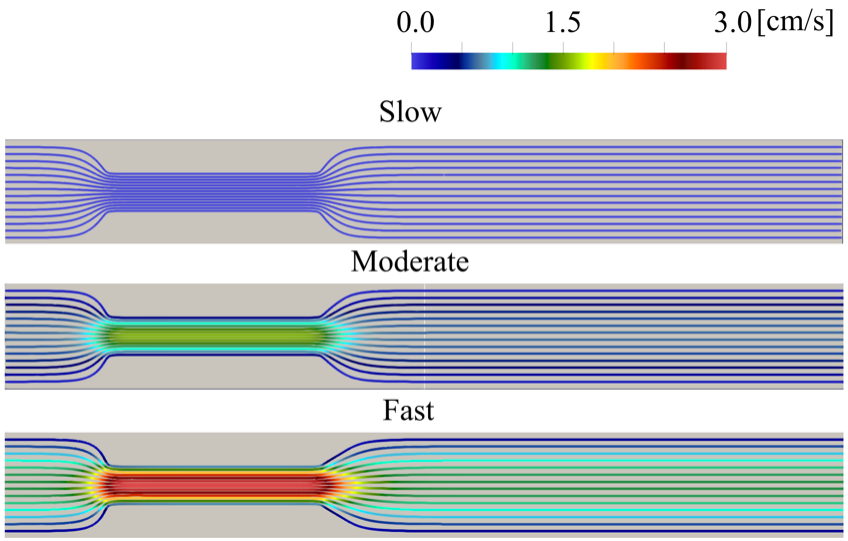

Figure 10: Velocity streamlines (cm/s) at t = 0.20 s

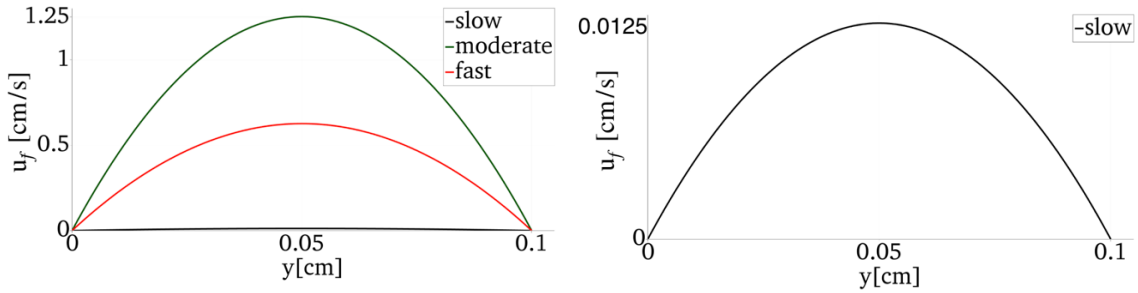

Figure 11: Velocity profile at the cross section of the tunnel at x = 0.01 cm and t = 0.20 s.

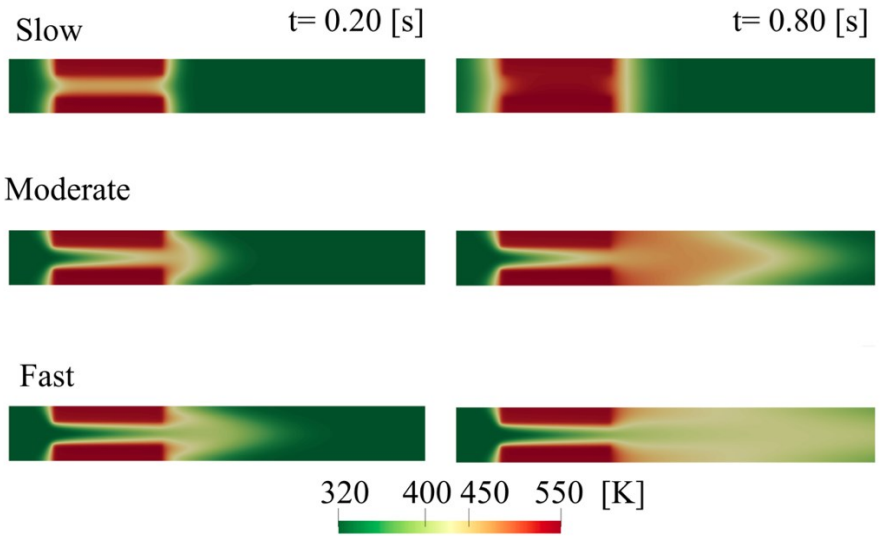

Figure 12: Temperature profile at different time steps (t = 0.20 and 0.80 s) for (a) slow, (b) moderate, and (c) fast flow fluid.

In Figure 12 we plot snapshots of the spatial distribution of the fluid temperature at different time steps to study the effect of the fluid velocity on the heat transfer. Here, the left side depicts the temperature profiles at $t = 0.20\,s$, whereas the right side shows the temperature profiled at $t = 0.80\,s$. It can be seen that the conduction process is dominant at low fluid velocity values (Figures 12 top), whereas for high fluid velocities, heat transfer is driven by the advection phenomena (Figures 12 middle and Figure 12 bottom, respectively).

4. TFSI SIMULATION OF IDEALIZED ROCKS IMMERSED IN A FLOW FLOW-CHANNEL

In this section we show a proof of concept towards the application of our TFSI method for simulating Enhanced Geothermal Systems (EGS). The set-up consists of two-dimensional idealized fracture asperities, which are immersed in a channel-flow. Although this is a very simplified representation of the physical processes of EGS, it enables to demonstrate the modeling capabilities of the proposed TFSI framework relevant for geophysics applications. In particular, the circulation of cold fluid, which is then heated by the hot rock mass.

We consider a more complex geometry consisting of four idealized fracture asperities which are immersed in a channel-flow. A fluid is pumped with velocity $v_m = 5\,cm/s$ and initial temperature equal to 323 K. The rocks are clamped at their bases (i.e. zero-displacements are prescribed), and have an initial temperature equal to 373 K. A constant temperature of 473 K is imposed on the top and bottom boundaries of the computational domain as depicted in Figure 13. The simulation set-up and material properties for the solid and the fluid domains are given in Figure 13 and Table 3. The fluid has a parabolic velocity at inlet defined as: $u_f = v_m(1.0 - y)y$, where u_f is the fluid velocity, y is the distance from the bottom of the channel, and $v_m = 0.3$ m/s.

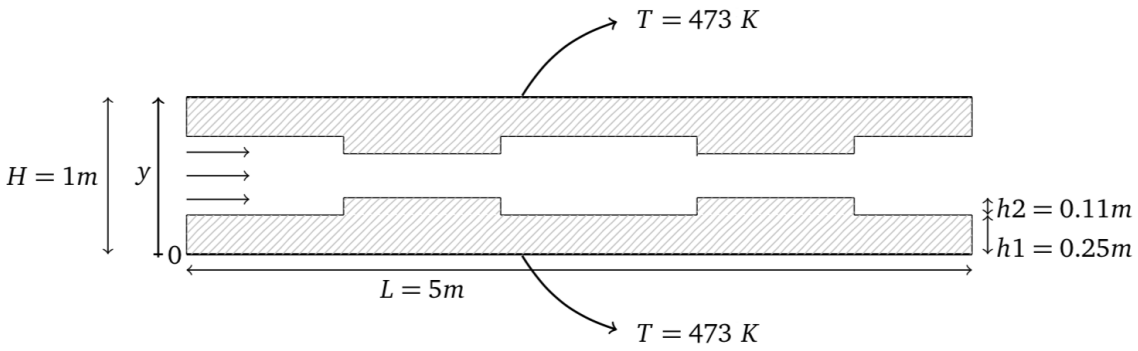

Figure 13: Set-up for the TFSI simulation of an idealized fracture geometry in a flow-channel.

In Figure 15, we analyze the temperature profile at x = 2.0 m, i.e. on the right of the first fracture aperture, at different time instants (t = 1.0, 2.0, 3.0, 4.0 s). Due to the concurrent heating processes, i.e. conduction and advection, the temperature of the fluid progressively increases until it achieves a value equal to 420 K. Such a trend can be also observed in Figure 16 where we show some snapshots of both the temperature and the fluid velocity in the flow channel. Here, we can see that the fluid velocity field increases in the narrow parts of the fracture. As a consequence, despite the low velocity profile prescribed at the inlet (Figure 14), the heat transfer is driven from both the diffusive and the advection phenomena, which makes this scenario more similar to the one analyzed in Figure 12 (middle row). On the contrary, close to the entrance the observed behavior is more similar to the one analyzed in Figure 12 (top row). Indeed, due to the small values of the fluid velocity field, the heat transfer is mostly driven by conduction and leads the fluid temperature to progressively increases before moving through the fracture asperities.

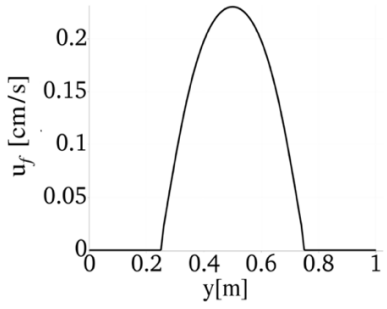

Figure 14: Velocity profile at the cross section of the tunnel at x = 0.01 cm and t = 0.20 s.

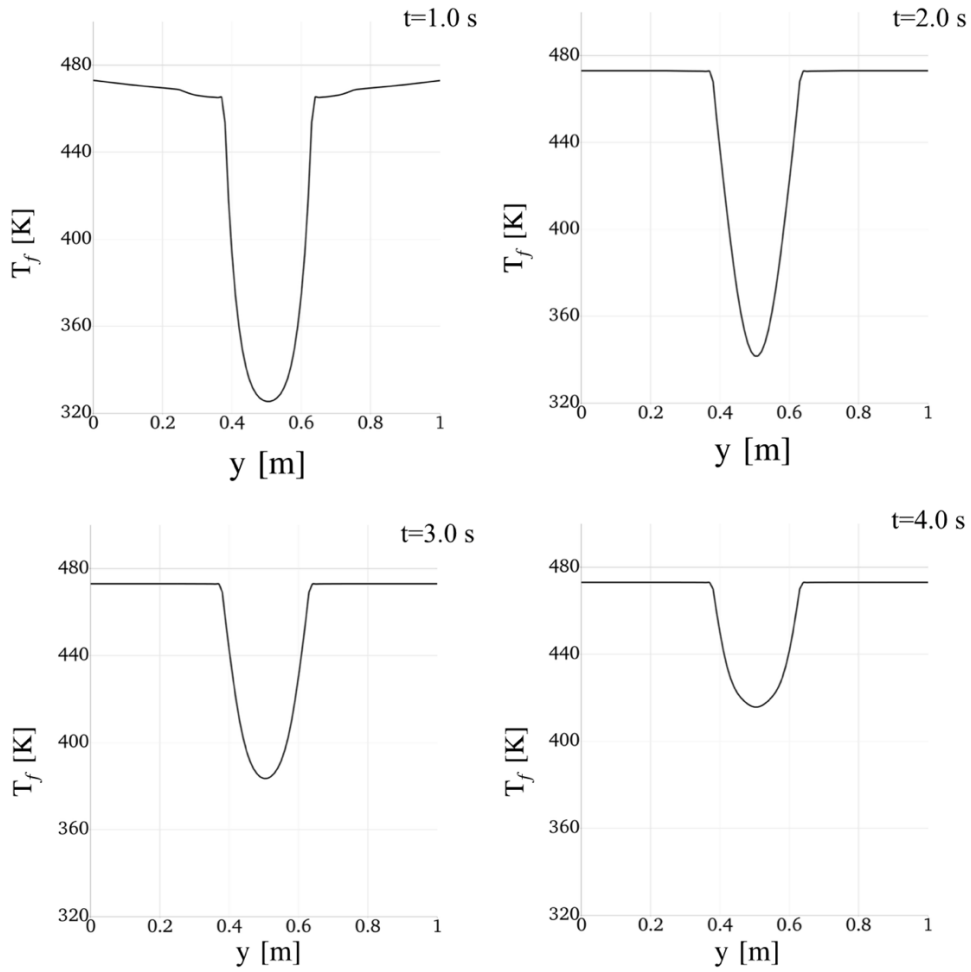

Figure 15: Temperature field analyzed on the right of the first fracture aperture (x = 2m).

5. CONCLUSION

In this paper, we presented a framework for the numerical simulation of fully coupled thermo-hydro–mechanical interaction based on the fictitious domain method. This approach simplifies the setup of TFSI simulations and allows us to solve coupled problems without an explicit representation of the complex boundary between two domains. First, we define the governing equations of linear thermo-elasticity to describe the heat transfer in a hot rock mass. Then, Navier-Stokes and energy equations are adopted to model the thermal phenomena in an incompressible Newtonian fluid. Finally, the two problems are coupled in a staggered manner by means of a penalty method based on the variational transfer. We verified the presented formulations with two-dimensional benchmarks on simple geometries. Then, we demonstrated that our methodology is capable of simulating the behavior of fluid flow and heat transfer in idealized two-dimensional fracture geometries. In summary, this article illustrates a proof of concept for the simulation of thermal-fluid-structure interaction in geothermal applications. Further investigations and numerical experiments will involve more complex three-dimensional geometries also including rough fracture surfaces.

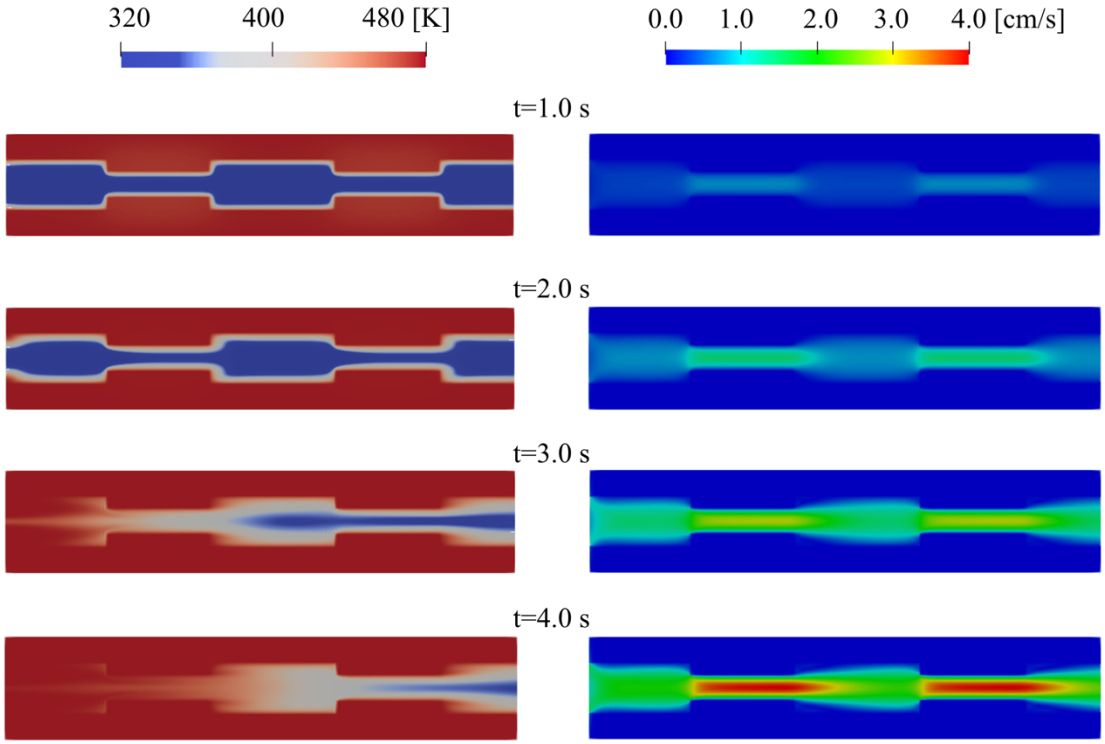

Figure 16: Snapshots of the simulation at different time instants of the temperature (left) and the velocity field (right).

REFERENCES

Alger, B., Andrš, D., Carlsen, R.W., Gaston, D.R., Kong, F., Lindsay, A.D., Miller, J.M., Permann, C.J., Peterson, J.W., Slaughter, A.E., and Stogner, R.: *MOOSE Web page*, (2019), https://mooseframework.org.

Anderson, J.D., and Wendt, J.: Computational fluid dynamics, *New York: McGraw-Hill*, **206,** (1995).

Boffi, D., and Gastaldi, L.: A finite element approach for the immersed boundary method, *Computers & structures*, **81,** (2003), 491-501.

Bond, A.E., Bruský, I., Cao, T., Chittenden, N., Fedors, R., Feng, X.T., Gwo, J.P., Kolditz, O., Lang, P., McDermott, C., and Neretnieks, I.: A synthesis of approaches for modelling coupled thermal–hydraulic–mechanical–chemical processes in a single novaculite fracture experiment, *Environmental earth sciences*, **76.1**, (2017), 12.

Cacace, M., and Jacquey, A.B.: Flexible parallel implicit modelling of coupled thermal–hydraulic–mechanical processes in fractured rocks, *Solid Earth*, **8.5**, (2017), 921–941.

Danowski, C., Gravemeier, V., Yoshihara, L., and Wall, W.A.: A monolithic computational approach to thermo- structure interaction, *International Journal for Numerical Methods in Engineering*, **95.13**, (2013), 1053-1078.

Donea, J., Huerta, A., Ponthot, J.P., and Rodríguez- Ferran, A.: Arbitrary Lagrangian–Eulerian Methods, *Encyclopedia of Computational Mechanics* Second Edition, (2017), 1-23.

Errera, M.P., and Duchaine, F.: Comparative study of coupling coefficients in Dirichlet–Robin procedure for fluid–structure aerothermal simulations, *Journal of Computational Physics*, **312**, (2016), 218-234.

Gaston, D., Newman, C., Hansen, G. and Lebrun-Grandie, D.: MOOSE: A parallel computational framework for coupled systems of nonlinear equations. *Nuclear Engineering and Design*, **239.10**, (2009), 1768-1778.

Glowinski, R., Pan, T.W., Hesla, T.I., and Joseph, D.D.: A distributed Lagrange multiplier/fictitious domain method for particulate flows, *International Journal of Multiphase Flow*, **25.5**, (1999), 755-794.

Hesch, C., Gil, A.J., Carreno, A.A., Bonet, J., and Betsch, P.: A mortar approach for fluid–structure interaction problems: Immersed strategies for deformable and rigid bodies, *Computer Methods in Applied Mechanics and Engineering*, **278**, (2014), 853-882.

Hsu, M.C., Kamensky, D., Xu, F., Kiendl, J., Wang, C., Wu, M.C., Mineroff, J., Reali, A., Bazilevs, Y., and Sacks, M.S.: Dynamic and fluid–structure interaction simulations of bioprosthetic heart valves using parametric design with T-splines and Fung-type material models, *Computational mechanics*, **55.6**, (2015), 1211-1225.

Kirk, B.S., Peterson, J.W., Stogner, R.H., and Carey, G.F.: libMesh: a C++ library for parallel adaptive mesh refinement/coarsening simulations, *Engineering with Computers*, **22.3-4**, (2006), 237-254.

Kopaničáková, A., and Planta, V.C.: *passo Web page,* (2018), https://scm.ti-edu.ch/projects/moose-passo.

Kornet, S., Ziółkowski, P., Jóźwik, P., Ziółkowski, P.J., Stajnke, M., and Badur, J.: Thermal-FSI modeling of flow and heat transfer in a heat exchanger based on minichanels, *Journal of Power Technologies*, **97.5**, (2018), 373-381.

Krause, R., and Zulian, P.: A parallel approach to the variational transfer of discrete fields between arbitrarily distributed unstructured finite element meshes, *SIAM Journal on Scientific Computing*, **38.3**, (2016), C 307-C333.

Li, S., Li, X., and Zhang, D.: A fully coupled thermo-hydro-mechanical, three-dimensional model for hydraulic stimulation treatments. *Journal of Natural Gas Science and Engineering*, **34**, (2016), 64-84.

Li, S., Feng, X.T., Zhang, D., and Tang, H.: Coupled thermo-hydro-mechanical analysis of stimulation and production for fractured geothermal reservoirs, *Applied Energy*, **247**, (2019), 40-59.

Lima, M.M., Vogler, D., Querci, L., Madonna, C., Hattendorf, B., Saar, M.O., and Kong, X.-Z.: Thermally driven fracture aperture variation in naturally fractured granites, *Geothermal Energy Journal*, **7.1**, (2019), 1-28.

Mittal, R., and Iaccarino, G.: Immersed boundary methods, *Annu. Rev. Fluid Mech*, **37**, (2005), 239-261.

Nestola, M.G.C, Gizzi, A., Cherubini, C., and Filippi, S.: Three-band decomposition analysis in multiscale FSI models of abdominal aortic aneurysms, *International Journal of Modern Physics C*, **27.02**, (2016), 1650017.

Nestola, M.G.C., Becsek, B., Zolfaghari, H., Zulian, P., De Marinis, D., Krause, R., and Obrist, D.: An immersed boundary method for fluid-structure interaction based on the variational transfer. Journal of Computational Physics, **398**, (2019).108884

Nowinski, J.L.: Theory of thermoelasticity with applications, *Sijthoff & Noordhoff International Publishers*, **3**, (1978).

Olasolo, P., Juárez, M.C., Morales, M.P., and Liarte, I.A.: Enhanced geothermal systems (EGS): A review, *Renewable and Sustainable Energy Reviews*, **56**, (2016), 133-144.

Peskin, C.S.: The immersed boundary method, *Acta numerica*, **11**, (2002), 479-517.

Peterson, J. W., Lindsay, A. D., and Kong, F.: Overview of the incompressible Navier–Stokes simulation capabilities in the MOOSE framework, *Advances in Engineering Software*, ***119***, (2018), 68-92.

Pironkov, P.: Numerical simulation of thermal fluid-structure interaction, *Doctoral dissertation*, Technische Universität, (2010).

Planta, C., Vogler, D., Nestola, M., Zulian, P. and Krause, R.: Variational parallel information transfer between unstructured grids in geophysics-applications and solutions methods. *In 43rd Workshop on Geothermal Reservoir Engineering, Stanford*, CA, (2018) 1-13.

Planta, C.V., Vogler, D., Chen, X., Nestola, M.G.C., Saar, M.O., and Krause, R.: Simulation of hydro-mechanically coupled processes in rough rock fractures using an immersed boundary method and variational transfer operators, *Computational Geosciences*, **23.5**, (2019), 1125-1140.

Saul'ev, V.K.: On the solution of some boundary value problems on high performance computers by fictitious domain method, *Siberian Math*. J, **4.4**, (1963), 912-925.

Smith, M.C.: The Los Alamos Scientific Laboratory Dry Hot Rock Geothermal Project/LASL Group Q-22, *Geothermics*, **4**, (1975), 27-39.

Taron, J., and Elsworth, D.: Thermal–hydrologic–mechanical–chemical processes in the evolution of engineered geothermal reservoirs, *International Journal of Rock Mechanics and Mining Sciences*, ***46.5***, (2009), 855-864.

Vogler, D., Settgast, R. R., Annavarapu, C., Madonna, C., Bayer, P., & Amann, F.: Experiments and simulations of fully hydro-mechanically coupled response of rough fractures exposed to high- pressure fluid injection. *Journal of Geophysical Research: Solid Earth*, **123.2**, (2018), 1186-1200.

Yin, Y., and Liu, Y.: FEM Analysis of Fluid-Structure Interaction in Thermal Heavy Oil Recovery Operations, *Sustainability*, **7.4**, (2015), 4035-4048.

Yu, Z.: A DLM/FD method for fluid/flexible-body interactions, *Journal of computational physics*, **207.1**, (2005), 1-27.

Zhang, L.T., and Gay, M.: Immersed finite element method for fluid-structure interactions, *Journal of fluids and structures*, **23.6**, (2007), 839-857.

Zulian. P.: ParMOONoLith: parallel intersection detection and automatic load-balancing library, *Git repository*, (2016), https://bitbucket.org/zulianp/par_moonolith.

Zulian, P., Kopaničáková, A., Nestola, M.G.C., Fink, A., Fadel, N., Magri, V., Schneider, T., Botter, E., Mankau, J., and Krause, R.: Utopia: A C++ embedded domain specific language for scientific computing, *Git repository*, (2016), https://bitbucket.org/zulianp/utopia.